HHS Public Access

Author manuscript

ACS Nano. Author manuscript; available in PMC 2018 March 28.

Published in final edited form as:

ACS Nano. 2016 October 25; 10(10): 9243–9258. doi:10.1021/acsnano.6b02776.

The Binding Site Barrier Elicited by Tumor-Associated Fibroblasts Interferes Disposition of Nanoparticles in Stroma-Vessel Type Tumors

Lei Miao[†], **Jay M. Newby**[§], **CMichael Lin**[†], **Lu Zhang**[†], **Feifei Xu**[§], **William Y. Kim**[‡], **MGregory Forest**[§], **Samuel K. Lai**[†], **Matthew I. Milowsky**[∥], **Sara E. Wobker**[⊥], and **Leaf Huang**[*,†]

[†]Division of Molecular Pharmaceutics and Center of Nanotechnology in Drug Delivery, Eshelman School of Pharmacy

[‡]Lineberger Comprehensive Cancer Center, University of North Carolina at Chapel Hill, Chapel Hill, North Carolina 27599, United States

[§]Departments of Mathematics and Applied Physical Science, University of North Carolina at Chapel Hill, Chapel Hill, North Carolina 27599, United States

[∥]Department of Medicine, University of North Carolina at Chapel Hill, Chapel Hill, North Carolina 27599, United States

[⊥]Department of Pathology, University of North Carolina at Chapel Hill, Chapel Hill, North Carolina 27599, United States

Abstract

The binding site barrier (BSB) was originally proposed to describe the binding behavior of antibodies to cells peripheral to blood vessels, preventing their further penetration into the tumors. Yet, it is revisited herein to describe the intratumoral cellular disposition of nanoparticles (NPs). Specifically, the BSB limits NP diffusion and results in unintended internalization of NPs by stroma cells localized near blood vessels. This not only limits the therapeutic outcome but also promotes adverse off-target effects. In the current study, it was shown that tumor-associated fibroblast cells (TAFs) are the major component of the BSB, particularly in tumors with a stroma-vessel architecture where the location of TAFs aligns with blood vessels. Specifically, TAF distance to blood vessels, expression of receptor proteins, and binding affinity affect the intensity of the BSB. The physical barrier elicited by extracellular matrix also prolongs the retention of NPs in the stroma, potentially contributing to the BSB. The influence of particle size on the BSB was also investigated. The strongest BSB effect was found with small (~18 nm) NPs targeted with the anisamide ligand. The uptake of these NPs by TAFs was about 7-fold higher than that of the other cells 16 h post-intravenous injection. This was because TAFs also expressed the sigma receptor

[*]**Corresponding Author**: leafh@unc.edu.

Supporting Information

The Supporting Information is available free of charge on the ACS Publications website at DOI: 10.1021/acsnano.6b02776. Additional detailed methodology including mathematical modeling, NP manipulation, Western blot, transgene expression, *etc.* are described in the methods section, and additional tables or figures are provided (PDF)

Notes

The authors declare no competing financial interest.

under the influence of TGF-β secreted by the tumor cells. Overall, the current study underscores the importance of BSBs in the delivery of nanotherapeutics and provides a rationale for exploiting BSBs to target TAFs.

Graphical abstract

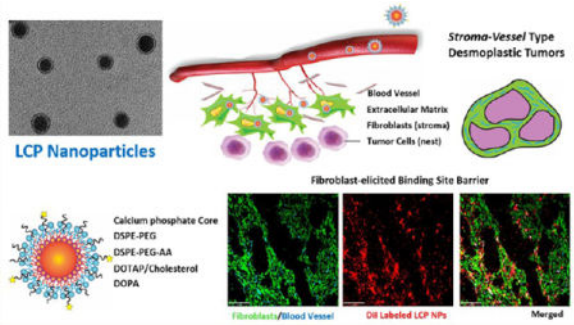

Keywords

binding site barrier; tumor-associated fibroblast; stroma-vessel type tumor; nanoparticle; desmoplastic tumor

The binding site barrier (BSB) hypothesis was originally proposed by Weinstein to explain the nonuniform distribution of monoclonal antibodies in tumor nodules.[1,2] Specifically, he proposed that cell populations localized near the blood vessels with high antigen density and binding affinity are likely to elicit a strong BSB.[1,2] Beyond affecting antibodies, the BSB may be extended to the intratumoral disposition of nanoparticles (NPs).[3] Unintended binding of NPs to cells near the blood vessels may significantly decrease the number of NPs available for penetration into the tumor matrix.[4] Considering the heterogeneous stromal cell populations around the blood vessels, unintended uptake of NPs into these cells constitutes the basis of off-target effects.[3,5]

Tumor-associated fibroblast cells (TAFs), including α smooth muscle actin (αSMA) or PDGFRα positive myofibroblasts, pericytes, and other mesenchymal peri-vascular cells, are the major component in desmoplastic tumor stroma and preferentially localize near blood vessels.[6] Multiple solid tumor systems such as pancreatic ductal adenocarcinoma (PDA), nonsmall cell lung cancer (NSCLC), aggressive urothelial carcinoma, and some breast cancers follow the aforementioned pattern, revealing TAFs as a major component of the BSB.[7–13] Previous studies conclude that TAFs can enhance cancer cell proliferation, invasion, and contribute to immune suppression.[14] Resultantly, the destruction of TAFs by exploiting their off-target NP localization has emerged as one potential therapeutic approach. The rationale states that the depletion of fibroblasts decreases the synthesis of extracellular matrix (ECM) proteins, downplaying mechanical barriers and facilitating drug delivery to tumor cells.[15,16] Yet, recent studies revealed the paradoxical and intricate role that TAFs play in constraining tumor growth. Specifically, the transgenic depletion of FAP positive fibroblasts actually facilitated tumor growth and metastasis in a PDA model, rather than suppression.[17–19] Furthermore, the off-target distribution of therapeutic agents to TAFs may

elicit paracrine secretion of survival factors such as Wnt16, promoting drug resistance in neighboring cells.[20,21] Moreover, TAF and tumor cell response to therapeutic agents is inconsistent across different models, leading to discrepancy in treatment outcomes.[7] Thereby, the investigation of fibroblasts and their role in the BSB is of great significance in understanding and solving the aforementioned off-target effects.

Herein, the fibroblast-elicited BSB for NP uptake was quantitatively investigated using lipid-coated calcium phosphate nanoparticles (LCP NPs). LCP NPs possess a steric surface with a brush PEG coating[22] and cationic lipid shell for enhanced uptake and release.[23] In addition, LCP NPs have demonstrated stable delivery of several modalities including macro-biomolecules and small phosphorylated drugs.[24,25] Therefore, LCP NPs were used to evaluate tumor perfusion and predict therapeutic outcomes. The influence of particle sizes on the BSB uptake was also investigated by tuning the surfactant ratio to prepare LCP NPs of various sizes.[26] Anisamide (AA), a model targeting ligand, was added on the surface of LCP NPs to evaluate the role of targeting ligands in dictating intratumoral cellular association of NPs.[27] To investigate the role of fibroblasts on the BSB, their distance to blood vessels, expression of receptor proteins, and binding affinity were studied. An *in vitro* tumor spheroid model was also established to evaluate the BSB. Based on the spheroid model, a mathematical model was created to assay the influence of each independent parameter. Overall, this study emphasizes the role of the BSB in dictating NP delivery and provides guidance for the design of therapeutic NPs to treat desmoplastic tumors.

RESULTS AND DISCUSSION

Characterization of LCP NPs

LCP NPs were prepared according to established protocols.[26] By adjusting the composition of the surfactant system, LCP core sizes could be tuned between 6 and ~50 nm. The hydrophobic DOPA-cores were further self-assembled with outer leaflet lipids to form the asymmetric lipid-bilayer NPs (Figure 1A–D). Sucrose-gradient centrifugation was used to purify LCP NPs. Approximately 0.5% DiI was incorporated into the outer leaflet to monitor the purification process. As shown in Figure S1, LCP NPs with dense CaP cores localized at the interface between the 10% and 20% sucrose layers. TEM imaging confirmed successful purification of LCP NPs. Particle size and surface modifications had minimal effect on purification efficacy as approximately 85% of DiI-labeled NPs were recovered consistently (Table S1).

Large LCP NPs (diameter ~65 nm and PDI ~ 0.3) are termed L-LCP NPs. Smaller LCP NPs (diameter ~18 nm and PDI ~ 0.2) are termed S-LCP NPs (Table S1). All NPs demonstrated a clear core/membrane structure as determined by TEM and presented similar zeta potentials ranging from 18 to 20 mV (slightly positive) due to cationic DOTAP (Figure 1 and Table S1). Structure and zeta potential were independent of particle size and particles maintained their diameters over 96 h (Figure 1E). NPs showed similar plasma clearance rates independent of size or the presence of targeting ligands (Figure 1F), consistent with studies using other NPs of different sizes and targeting motifs.[28,29] To confirm that outer leaflet lipids containing DiI served as a feasible tracker, the integrity of NPs before cellular internalization was determined *in vivo*. A hydrophilic Texas Red Oligo was encapsulated

into the CaP core along with hydrophobic DiI in the outer leaflet of L-LCP NPs. The fluorescence intensity of each dye remained similar when loaded alone or simultaneously into the NPs, suggesting little to no intermolecular Förster resonance energy transfer (FRET) interference between two fluorophores (Figure S2). Therefore, co-expression of Texas Oligo and DiI in an individual tumor cell after systemic circulation is an indication of NP integrity. Flow cytometry analysis indicated that ~15% of cells in the tumor tissue co-expressed the aforementioned two fluorophores within 16 h after injection of the double-labeled NPs (Figure 1G), accounting for ~70% of all the fluorescence positive cells. Dissociated single-dye positive cells were observed 28 h post-injection, likely due to dissociation of NPs trapped in the ECM or intracellular degradation of released fluorophores. Data herein suggest that DiI localized in the outer leaflet remains associated with the inner core within 16 h during systemic delivery. The co-localization of these two fluorophores was also visualized by confocal microscopy (Figure 1H). The majority of these dyes localized in the GFP positive stromal region near tumor vasculature, while only a small portion was observed in other cells. Thus, size tunable DiI-labeled LCP NPs were suitable for the evaluation of NP size or surface properties on intratumoral cellular distribution (within ~16 h post-injection).

Binding Site Featured by TAFs within the Stroma-Vessel Type Tumors Affects the Intratumoral Disposition of Nontargeted NPs at Early Time Points

The role of stromal patterns on the intratumoral distribution of NPs was investigated. Based on the anatomical architecture and the relative location of blood vessels and fibroblasts within the tumor, we categorized malignant solid tumors into two phenotypes: the stroma-vessel type and tumor-vessel type. Similar criteria were also used by Smith *et al.* to classify tumors.[7] Although discrepancies exist between our observations and theirs with respect to several biological parameters, the anatomical classification is very similar, if not identical. We classified a less desmoplastic NSCLC H460, a more sclerotic-like 4T1 breast cancer,[30] and a BXPC3 desmoplastic pancreatic tumor[28] as tumors with stroma-vessel architecture. Pathologies (Figure 2A, Table S2, and Figure S3) suggest that αSMA positive fibroblasts are localized near blood vessels within the well-developed collagen-rich stroma area in all three tumors. Despite the discrepancies in blood vessel densities, collagen depositions, and interstitial fluid pressure (IFP), these three models meet the basic criteria of stroma-vessel type tumors. Immunofluorescence staining (IF) also indicated the formation of tumor nests. This is in comparison to melanoma tumors such as D4M and A375lu where tumor vessels are embedded throughout the tumor cell mass, revealing a tumor-vessel phenotype (Figure 2A). The influence of stromal architecture on NP dispositions would be best visualized in animals bearing two tumor phenotypes and treated with highly permeable NPs with minimal selective cellular binding. Further, the difference should be magnified at earlier time points.[2] Therefore, D4M, H460 and BXPC3 were used as model tumors in animals treated with nontargeted S-LCP NPs and examined 8 h after injection. The representative images are shown in Figure 2B. Since these tumors vary in blood vessel perfusions and IFP, results should be interpreted with caution. Yet, the percolation of S-LCP NPs from blood vessels into both αSMA positive and negative areas was observed in the tumor-vessel phenotype tumor, D4M. Only 12.4 ± 6.2% DiI S-LCP was found in the stroma area. Meanwhile, the majority (65.3 ± 8.9% and 58.6 ± 7.5%) of DiI-positive S-LCP NPs were trapped in the

stroma of stroma-vessel type H460 and BXPC3, respectively. Therefore, proximity of stromal components to blood vessels likely dictates the distribution of nontargeted NPs in regions of dense stroma in stroma-vessel type tumors.

Mechanical barriers such as tight junctions, ECM, or elevated IFP can trap nontargeted NPs in the noncellular stroma.[1] The binding and internalization of NPs in the cellular compartment of the stroma, *i.e.* BSB, also depletes the NPs. To examine the role of BSB in stromal cells, the association of DiI-labeled NPs with major stromal cells, *i.e.*, fibroblasts, was investigated. Individual cells were collected after tumor tissue digestion and labeled with anti -αSMA or -PDGFRα, two markers commonly used for a wide population of fibroblasts (TAFs).[31] After staining, samples were studied with flow cytometry, and results were shown in Figure 2C. In stroma-vessel type tumors (both H460, 4T1, BXPC3), association of DiI NPs (S/L) with αSMA positive cells was ~2- to 3-fold higher than those delivered to the tumor nests. The trend was similar in fibroblasts labeled with PDGFRα (Figure S4). Stroma densities varied among tumors (*i.e.*, 4T1 and BXPC3 having more stroma than H460), but the preferential distribution of NPs in stroma remained constant. Consistent with previous findings, smaller NPs demonstrated higher association with total cells, but the association ratio between fibroblasts and other cells (mainly tumor cells) was independent of size. However, the trend was reversed in the tumor vessel models (D4M and A375lu), where tumor cells favored DiI NPs' accumulation. The data suggest that the binding site characteristic of fibroblasts was independent of particle size and stroma density, but strongly dependent on anatomical position of blood vessels.

To minimize the interference of heterogeneity in fibroblasts and the nonspecific staining using antibodies, a xenograft model consisting of the GFP-transfected NIH3T3 fibroblasts (3T3-GFP) and human bladder cancer UMUC3 was established. Since this model contains few host fibroblasts[16] (Figure S5), the introduction of exogenous 3T3 fibroblasts minimizes the heterogeneity of TAFs. It was found that this bladder tumor mainly adopted a tumor-vessel structure when smaller than 200 mm^3. The tumor then transitioned to a stroma-vessel structure when larger than 400 mm^3 (Figure 3A). Consistent with the previous results, NPs of all sizes tested localize preferentially to fibroblasts in large tumors (Figure 3B). Double staining of blood vessels and TAFs in patient bladder cancer tumor microarray (TMA) cores ($n = 40$) suggests that ~80% of the desmoplastic tumor cores have a stroma-vessel architecture distinguished by prominent tumor nests, which was similar to the artificial large UMUC3/3T3 tumors (Figure S6). Furthermore, the S-LCP NPs also preferentially localized to TAFs in a patient-derived xenograft bladder cancer model (PDX model) (Figure 3C). All these indicate that the artificial large-size UMUC3/3T3 model accurately simulates NP disposition with high clinical relevancy. Herein, our findings demonstrate the binding site characteristics of fibroblasts in stroma-vessel tumors affect the initial distribution of non-targeted NPs. Since stroma-vessel tumors often indicate poor patient prognosis, further studies on these tumor subtypes were conducted using UMUC3/3T3 (>400 mm^3, ~30% fibroblasts) as a standard model.

Fibroblast-Induced BSB Was Intensified and Prolonged for Targeted NPs in Stroma-Vessel Type Tumor Models

AA has been exploited for targeted delivery of NPs to many epithelial cancers overexpressing the sigma receptor (Sigma R).[24,27,32] To assess whether AA could increase binding affinity of LCP NPs to tumor cells and overcome the fibroblast-mediated BSB, the intratumoral dispositions of NPs with or without AA were examined. Eight % of AA (40% of the total DSPE-PEG) was coated onto the surface of NPs to ensure enhanced cellular uptake while maintaining the same physicochemical properties (Figure 1E,F, Table S1). Some molecularly targeted NPs have been reported to provide prolonged retention in tumor tissue, suggesting a delayed tumor clearance due to high binding affinities.[4,29,33] Therefore, the kinetics of AA-targeted and nontargeted LCP NPs' were determined. Accumulation of ^{3}H-labeled particles in UMUC3/3T3 was quantified for 16 h after intravenous injection, before NPs were degraded (Figure S7A). Results suggest that the tumor accumulation kinetics were roughly identical for particles with or without AA. However, smaller NPs demonstrated greater tumor accumulation compared to large NPs. In all four cases, tumor levels of NPs increased rapidly during the initial 8 h to 5–8% injected dose/g tumor tissue and remained steady over the next 8 h. No significant NP clearance was observed during the time monitored. Although tumor levels of targeted NPs were somewhat higher than those of the nontargeted NPs at certain time points, these differences were not significant ($P > 0.05$), which was consistent with Kirpotin *et al.* observation using antibody modified liposomes.[34] While the result is somewhat counterintuitive, the AA modifications indeed increased the cellular association of NPs within tumor tissues (Figure S7B).

The time-dependent cellular association of NPs (DiI labeled) in GFP positive fibroblasts and other cell populations was further measured by flow cytometry and compared. Although the overall tumor accumulation is similar, the cellular localization of AA LCP NPs and its nontargeted counterpart is fundamentally different. Data in Figure 4A show that nontargeted NPs appeared in GFP positive fibroblasts first, before they appeared in other non-GFP-labeled cells, suggesting the gradually extravasation of NPs from the stromal layer, despite the presence of BSB. Consistent with other studies, S-LCP NPs were preferentially internalized by cells over L-LCP NPs. Sixteen hours after injection, over 40% of cells containing S-LCP NPs were nonfibroblast cells, and over 30% of nonfibroblast cells were DiI-positive. Surprisingly, the addition of AA did not increase the ratio of DiI-positive nonfibroblast cells. Rather, the initial association ratio of NPs (both S and L) with fibroblasts increased almost 2-fold over nontargeted NPs and was plateaued over 16 h (Figure 4A). Flow cytometry alone is insufficient to show the spatial information on NPs, so the preferential association of targeted NPs within stroma was further confirmed by fluorescence imaging (Figure 4B). Low-power magnification fluorescent images show that nontargeted S-LCP NPs, in particular, expanded across the stroma and penetrated deeper into the tumor nests at 16 h post-injection. In contrast, the stromal matrix was populated with targeted NPs, leaving minimal distribution in the GFP negative area (Figure 4B). We also observed that the S-LCP NPs demonstrated a disperse distribution pattern compared to L-LCP NPs. Perhaps, either uneven blood vessel permeability or differences in the ECM composition may have limited the distribution of large NPs.

The intratumoral diffusion kinetics of S-LCP NPs (two determined time points) was visualized by the higher magnification images (Figure 4C). CD31 (shown as cyan) was used to outline the blood vessel. It can be seen that, at 4 h, both AA targeted and nontargeted NPs mainly resided within or near the blood vessels. While at 16 h, only nontargeted NPs penetrated the stroma layer and diffused deep into the tumor nests. Consistent with the fluorescence images, quantitative analysis of the tumor penetration (Figure 4D) suggests that the distribution radius of DiI positive cells increases over time in nontargeted NPs, but not the targeted group (Figure 4D). The quantification of DiI percentages and intensities in the stroma area and tumor nest agreed with the above observations. Collectively, our results suggest that for tumors with slow clearance, targeting ligands are not supposed to affect the retention of NPs, but they do significantly affect NPs' uptake in stroma and tumor cells, along with the penetration into tumor nests. Specifically, we found that the fibroblast-mediated BSB was intensified and prolonged when NPs were modified with AA.

Intratumoral Cellular Association of S-LCP NPs (with or without AA) in the UMUC3/3T3 Xenografts

High-resolution confocal microscopy was used to identify the uptake of NPs within different cell populations. Tumor cells were pretransferred with GFP (UMUC3-GFP, shown as magenta), while fibroblasts were prelabeled with RFP (3T3-RFP, shown as green) to distinguish these two cell populations within the tumors. Data in Figure 5A suggest that UMUC3 cells constitute the majority of the nonfibroblast cells. As expected, nontargeted S-LCP NPs were detected within tumor cells 16 h post-injection, as illustrated by the co-localized pink color in the tumor cell cytoplasm (Figure 5A(a)). Minimal nontargeted NPs were co-localized within or near the CD31 positive endothelial cells (Figure 5A(c)), suggesting that interaction of NPs with the anionic endothelial glycocalyx was negligible due to the high-density PEG shielding effects.[35] In contrast, the intracellular localization of targeted LCP in tumor cells was a rare event. Even when observed, particles only concentrated in tumor cells next to fibroblasts. The accumulation of targeted LCP, however, was extremely high near the blood vessel. This may be attributed to the binding of NPs to pericyte-like and perivascular fibroblasts, demonstrating a strong BSB which occurred rapidly when NP extravasated from blood vessels (Figure 5A).

Since infiltrating leukocytes (including neutrophils, lymphocytes, macrophages, *etc.*) also constitute the TME, their contributions to off-target effects were also investigated. Confocal images suggest that CD45 positive leukocytes account for approximately 11% of total cells within UMUC3/3T3 xenografts (Figure 5B). As expected, limited nonspecific uptake of NPs (with or without targeting ligand) was observed, further inhibiting NPs from approaching the tumor nests. Results of flow cytometry was consistent with images and demonstrated NP association with CD45-positive leukocytes varied among the tested tumor models (Figure S8). No significant trend of NP uptake was observed in terms of different phenotypes and targeting ligands. This finding highlights the premise that the primary BSB in the selected models is composed of TAFs.

Increased Expression of Sigma Receptor in TAFs Resulted in the Enhanced BSB for Targeted NPs

The distribution of Sigma R was then evaluated by co-immunostaining Sigma R with GFP-positive fibroblasts, CD31 or αSMA. Results in Figure 6A demonstrated a heterogeneous Sigma R distribution. Tumor cell-rich areas were primarily Sigma R-positive, whereas, CD31-positive endothelial cells were not. However, the distribution of Sigma R was uneven among GFP-fibroblasts (Figure 6C). Primarily, the expression of Sigma R was greater in αSMA-positive fibroblasts than αSMA-low fibroblasts (Figure 6B,C). Consistently, other tumor models, 4T1, A375lu, and H460 (Figure 6D–F) expressed different levels of Sigma R in the αSMA-positive activated fibroblasts as indicated by the numbers in the figure, suggesting that the expression of Sigma R positive fibroblasts was not unique to the mixed bladder cancer xenografts. Furthermore, we found that under normal conditions, the expression of Sigma R in fibroblasts (*e.g.*, NIH3T3, MRC5, WI-38) was constantly low compared to tumor cells, consistent with previous findings (Figure 6G). Therefore, the use of AA-mediated targeting was initially believed to be beneficial to tumor specific targeting. Yet, fibroblasts activated by TGF-β (TAFs) showed increased αSMA and Sigma R expression over time (Figure 6H). Further, activated fibroblasts demonstrated consistently higher uptake efficiency for targeted, but not untargeted NPs compared to unactivated fibroblasts (Figure S9). Therefore, activated TAFs expressing higher levels of Sigma R induced enhanced uptake of NPs and led to an intensified BSB.

To confirm the aforementioned hypothesis, individual cells in tumor tissues were collected 8 h post-NP injection for Sigma R staining and flow cytometry. To exclude interference from other stromal cells, the tumor cells were pretransfected with fluorescent GFP. As shown in Figure 7A–E, the association of NPs with cells increased with the expression of Sigma R. Consistent with previous findings, the fibroblasts were categorized based on the expression level of Sigma R, into Sigma R (−), Sigma R low (L), and Sigma R high (H) (Figures 7C and S10). Next, a fibroblast cell strain expressing shRNA specific to Sigma R to block induction of Sigma R expression was generated (Figure 7F). 3T3-GFP (shRNA Sigma R) cells were mixed with UMUC3 and inoculated, low to no level of Sigma R expression of fibroblasts in the knockout model was confirmed (data not shown). As expected, the disposition of IV administered AA-targeted NPs in Sigma R knockout fibroblasts was significantly decreased, while association of NPs with tumor cells increased compared to standard UMUC3/3T3 model (Figure 7G). Thus, specific AA–Sigma R interactions facilitated the BSB in fibroblasts for targeted NPs.

High Binding Affinity Explains the Intensified BSB for AA-Targeted NPs

The binding affinity of NPs to fibroblasts and tumors is a direct indicator of the BSB strength.[1] As described above, fibroblasts possess a heterogeneous expression of Sigma R *in vivo*. Thereby, to relate the NPs binding properties in activated NIH3T3 *in vitro* with the average behavior of *in vivo* TAFs, GFP-positive fibroblasts were sorted from the tumor tissue by MoXlo Flow. The binding affinity of AA LCP NPs was determined with these sorted fibroblasts and found to be identical to their binding affinity to NIH3T3 activated with TGFβ for 24 h *in vitro* (Figure 8A). The binding constants (K_D) of both nontargeted and targeted NPs were then compared *in vitro* on this activated NIH3T3 and UMUC3 cells. As

shown in Figure 8B, both UMUC3 and NIH3T3 did not bind with any nontargeted NPs. Yet, AA-modified NPs bound strongly with both UMUC3 and activated NIH3T3 at low concentrations. Binding plateaued as the particle number increased. The apparent K_D of AA L-LCP NPs for UMUC3 and activated NIH3T3 was 11.13 and 10.11 nM, respectively. Low and comparable dissociation constants suggested strong and similar binding affinities for both types of cells. The binding capacity of UMUC3, indicated by the surface saturation level, was higher compared to the activated NIH3T3. This finding is consistent with the fact that higher levels of Sigma R are present on UMUC3 over a majority of the activated fibroblasts even though the Sigma R was upregulated in TAFs (Figure 8B).

In most cases, NPs entered cells following binding to the cell surface. Thereby, the uptake process including adhesion and internalization was further evaluated on both fibroblasts and tumors. As expected, the targeted NPs entered cells more rapidly regardless of size compared to nontargeted NPs, likely due to the facilitated ligand–receptor interaction process. Consistent with the previous hypothesis describing a necessary wrapping time of the membrane, larger NPs required stronger driving forces and additional energy for successful cellular internalization.[36,37] Therefore, cellular uptake quantities of NPs decreased with increasing particle size. Additionally, similar linear uptake profiles were observed between the two cell types (Figure 8C,D). The uptake rates for the targeted NPs in these two cell lines were almost identical. Meanwhile, the uptake rate was slightly higher in UMUC3 than in the activated fibroblasts with nontargeted NP (Figure 8C,D). Altogether, observations herein demonstrated that targeted NPs with high avidity can bind rapidly to and be taken up by nontumor cells expressing lower levels of Sigma R. Subsequently uptake is sufficient to elicit a BSB.

In Vitro Tumor Spheroid Modeling of the BSB

To quantify the BSB *in vitro*, a spheroid model was generated in which tumor cells (UMUC3) were enclosed by fibroblasts (3T3-GFP) to simulate the *in vivo* condition. The core–shell structure was confirmed by confocal Z-stack scanning from the bottom to the center of the spheroid with each layer measuring 15 μm in thickness (Figure S11A). Images indicated that the overall diameter and the fibroblast-shell thickness increased as the amount of added fibroblasts increased (Figure S11B,C). The core–shell 3D model (35% fibroblasts) closely mimicked the *in vivo* condition of the UMUC3/3T3 model where a single tumor nest was surrounded by a thin layer of stroma cells (Figure S11B). Thereby, this model was used to analyze the real-time disposition of NP into tumor nests after their extravasation from blood vessels.

An excess of DiI-labeled LCP NPs (S/L, ±AA) was incubated with the 3D spheroids in 37 °C under frequent stirring. The spheroids were imaged at determined time points approximately 150 μm from the bottom of the spheroid (Figure 9A). Background fluorescence was corrected by subtracting the fluorescence at 0 h. Consistent with the *in vivo* study, the use of targeting ligands had a pronounced effect on the penetration of NPs in the spheroid. DiI-labeled AA S-LCP NPs and L-LCP NPs bound rapidly to the surface of fibroblasts within 30 min after incubation. Upon binding, the fluorescence intensity of targeted NPs in the fibroblast region increased with time. However, penetration into the

tumor nest required nearly 6 h post-incubation before a notable amount was observed. On the other hand, nontargeted NPs required longer incubations before initial binding. Yet, fluorescence penetrated rapidly into the tumor nest upon binding, resulting in the illumination of the entire nest soon afterward. These dynamics were further observed by averaging the intensities in the fibroblast (Figure 9B,C, gray zone) and tumor cell regions. For targeted NPs, the fluorescence intensity in the fibroblast region was approximately 4 times higher than that in the tumor region, demonstrating lower penetration of targeted NPs. Time-dependent accumulation of nontargeted NPs in the fibroblasts region of the spheroid was notably similar to targeted NP except for the delayed binding. However, the behavior was different in the tumor region, in which the fluorescence intensity increased monotonically and eventually closed to the intensity in the fibroblasts region. Together, these observations are consistent with the *in vivo* observation and demonstrate that the fibroblasts served as the primary barrier for NPs penetration, especially for targeted NPs. The distribution of large NPs was similar to the small NPs but significantly smaller in signal strength, suggesting the role of particle size in tumor penetration.

Mathematical Model: Mechanical Barrier Strengthens the BSB

We developed a mathematical model to examine the contribution of NP diffusion through the extracellular matrix and uptake by cancer cells or fibroblasts on the distribution of different NPs in the aforementioned 3D spheroid model. Assuming the diffusivity of S-LCP is constant throughout this single-cell population spheroid, we obtained the best fit to the experimental data when $D = 3.1 \times 10^4\ \mu m^2/h$ and $k = 0.25\ h^{-1}$ (Figure 10A), comparable with those of 12 nm cationic quantum dots or 20 nm PEGylated polymeric NPs measured in collagen gels mimicking the ECM reported elsewhere.[38,39] These results suggest that the uptake kinetics of S-LCP NPs is slow enough to allow them sufficient time to diffuse deep into the tumor spheroid before internalizing into cells.

We next sought to investigate the impact of the uptake *vs* diffusion on the intratumoral distribution of AA S-LCP NPs in the same UMUC3 only spheroid model (Figure S12). Since AA presumably does not directly interact with extracellular matrices, and given that AA S-LCP possessed identical size, surface charges, and PK profiles as S-LCP, we assigned the same diffusivity value ($3.1 \times 10^4\ \mu m^2/h$) for AA S-LCP NPs. Unlike the relatively uniform distribution of S-LCP NPs, AA S-LCP NPs were primarily localized at the GFP-edge, presumably due to increased uptake rates of AA S-LCP in cancer cells. Indeed, assuming the increased uptake rate for AA S-LCP NPs relative to S-LCP is comparable to what we observed *in vitro* on a monolayer culture of UMUC3 (Figure 8C,D), the NP distribution predicted by the model appeared to reasonably match experimental data (Figure 10B) and underscore that uptake kinetics for AA-conjugated NP is comparable if not faster than the diffusion kinetics.

Interestingly, the localization of AA S-LCP in the 3D spheroid periphery was more pronounced in UMUC3/3T3 spheroids. Preliminary studies suggest that the fibroblasts' expression of Sigma R was consistent to that quantified *in vivo* over the course of measurement (data not shown), and we observed similar NP uptake rates in fibroblasts *vs* UMUC3 in monolayer cell cultures *in vitro* (Figure 8C). These results suggest BSB is most

likely attributed in part to decreased diffusivity of NPs in the fibroblasts layer (Figure 10C). With the decreased diffusivity, the time it takes for NPs to diffuse through the fibroblasts layer increases, which further increased fraction of NPs internalized into the fibroblasts and intensified the BSB (Figure 10E,F). This prediction was confirmed by examining the ratio between the MFI of DiI in fibroblast layer and the tumor layer of the two spheroid models using flow cytometry (Figure S13).

CONCLUSIONS

In summary, a detailed investigation into the BSB elicited by TAFs and the subsequent effects on intratumoral deposition of sub-100 nm NPs in a stroma-vessel tumor model was conducted. Results herein focus on characterization of the TAF-elicited BSB through three major qualities defining the BSB: the proximity of the TAFs to blood vessels, the number of Sigma R, and the binding affinity.[1]

First, the close proximity of fibroblasts to blood vessels in stroma-vessel type tumors contributed to the role of TAFs as a binding site for NPs. Data herein suggested that NPs preferentially distributed to fibroblasts initially, regardless of size or the presence of targeting ligands, resulting in depletion of NPs available for tumor uptake. While the biological mechanism for the formation of this stroma-vessel architecture is unknown, it is conceivable that fibroblasts infiltrate during desmoplasia and envelop the neoplasm, subsequently influencing the architecture.[9] Although blood vessels are sometimes observed in the tumor nests, the extravasation of NPs within the tumor nest was still reduced by the malfunction of intranest blood vessels.[28]

The number of receptors characterizes a second feature of the BSB. Overexpression of Sigma R is reported in several fast growing cancer cell lines. Since TAFs are metabolically active compared to quiescent fibroblasts, increased expression of Sigma R is reasonably consistent with previous investigations demonstrating the up-regulation of Sigma R in rapidly dividing normal tissues.[14,40] Consistently, both the up-regulation of Sigma R and its heterogeneous distribution could be correlated with αSMA expression and triggered by TGFβ. The overexpression of Sigma R on TAFs was also observed in several patient bladder cancer samples (Figure S14), unveiling the clinical relevancy of this finding. As expected, AA (ligand of Sigma R) targeting paradoxically strengthened the BSB elicited by fibroblasts for NPs. This off-target binding of NPs to stroma cells was not the only challenge for AA coupled NPs. Other targeting receptors whose expression correlates with metabolic rate (*e.g.*, folate and transferrin receptors) also exist in nontumor cells and are likely prone to unspecific targeting.[3,41,42] Since these ligands are commonly used for tumor-targeted therapy, evaluation of off-target distribution would be of significance for therapeutic guidance.

While the induced expression of Sigma R in TAFs is still somewhat lower than in cancer cells, a strong binding affinity of NPs to TAFs constitutes the third parameter of the BSB. Notably, the high avidity of targeted NPs to TAF receptors compromises selectivity based on the number of receptors per cell, as NPs can bind rapidly with fibroblasts expressing lower levels of receptor.

Mathematical modeling based on the *in vitro* spheroid model demonstrated that the observed BSB is attributed to both enhanced binding and uptake of AA-conjugated NPs as well as reduced diffusivity of NPs through the TAF layer; the reduced diffusivity further maximizes the fraction of NPs that can bind and internalize into TAFs. Factors such as the highly packed extracellular proteins secreted from TAFs, the spindle shape of TAFs, the presence of tight junctions, and the raised IFP could all contribute to the decreased diffusivity of NPs across TAFs.[5,39,43] It should be noted that the BSB phenomenon is not unique to TAFs and can likely be extended to various types of cells (including tumor cells), since we also observed preferential distribution of NPs in the tumor periphery even with a purely tumor-cell spheroid. However, the tumor cell-elicited BSB is weaker, in part due to the relative higher NP diffusivity in these cells as compared to TAFs, further illustrating the importance of TAFs as a strong BSB. Although the *in vitro* spheroid model and mathematical modeling did not consider the extravasation of NPs from blood vessels along with the shape and volume of the tumor nests, the current modeling and quantification still parallel the experimental observations. In particular, the MFI (of DiI) in the stroma layer was almost 4-fold higher than that of the tumor nests 12 h post AA S-LCP incubation *vs* almost 1 after S-LCP incubation in the 3D spheroid model. This finding mirrored the quantification obtained 16 h after IV injection of LCP NP *in vivo* (Figure 4C,E). Therefore, the similarity between the *in vitro* model and *in vivo* quantitation demonstrates the relevance of the spheroid model, particularly for simulating the BSB.

Admittedly, the actual tumor microenvironment in different tumors is too complicated to be precisely represented by this single mathematical model. For example, this mathematical modeling cannot be applied to tumors with limited vessel permeability, where transvascular transport would be a hindrance for NP delivery. In addition, it also need to be expanded to account for nonspherical shape of tumor spheroids, heterogeneity within the spheroid, and variations in the diffusivity due to ECM and cell density when simulating the actual tumor models *in vivo*. However, to our knowledge this is the first model discussing fibroblast-mediated BSB for NPs. It provides qualitative guidance and reasonable quantitative accuracy as a first approximation.

Consistent with other studies, this study suggested that nontargeted NPs demonstrated favorable tumor penetration over targeted NPs. The association of nontargeted NPs to tumor cells was actually higher than for targeted NPs over time, opposing the dogma that nontargeted NPs have greater penetration but lower cellular uptake. Compared to other studies using neutral or anionic NPs (*i.e.*, gold NPs,[44] hydrogel NPs,[45] polymeric micelles,[28] *etc.*), cationic PEGylated NPs were studied herein. Undoubtedly, surface charges affect the penetration and uptake of NPs. For example, nontargeted anionic particles are more likely to penetrate deeper into the tumor. However, their efficacy is limited by insufficient cellular uptake. Meanwhile cationic NPs accumulate within the endothelium which limits penetration, whereas, highly PEGylated cationic NPs were used in the current study, decreasing endothelial binding due to PEG shielding while demonstrating greater uptake than anionic NPs. Previous studies demonstrated that shedding of the PEG layer on DOTAP-coated NPs causes a subsequent shift in the PEG confirmation from brush to mushroom. This shift exposes cationic charges and enhances cellular uptake, offering a potential explanation for the greater cellular uptake observed in the current study.[46]

What, then, is the significance of studying the TAF-elicited BSB? The TAF-elicited BSB depletes the number of NPs available to tumor cells, compromising therapeutic efficacy. Simultaneously, TAF depletion further induces adverse effects due to resistance of stromal cells to tumor-specific therapy. Examples of adverse effects can be found in a previous study, where TAF internalization of cisplatin NPs induced the secretion of Wnt16 (a survival factor) and paradoxically promotes tumor growth and metastasis.[20] Despite certain limitations and assumptions, this study demonstrates the mechanistic basis of these off-target effects from the aspect of NP-delivery and offers guidance for the development of nanotherapeutics against stroma-vessel desmoplastic type tumors. Separately, these findings explore the rationale of intentionally targeting fibroblasts through the BSB. This fibroblast-specific targeting feature of the NPs can be utilized to deliver reagents specifically to TAFs, reprogramming the stroma from tumor supportive to tumor inhibitive,[47,48] to exploit TAFs as an *in situ* cytokine or cytotoxic protein producing reservoir, overcoming the tumor-specific delivery barrier, orchestrating the suppressive tumor microenvironment, and improving the currently marginal antitumor outcome of stroma-vessel type tumors.

METHODS

Preparation of Fluorescently Labeled LCP NPs

The LCP NPs were prepared using a previously described method with some adjustments.[26] Additional details of NP manipulation are provided in the Supporting Information. To label the final LCP NPs, 0.5% DiI (mol/mol) was mixed with the outer leaflet lipid solution before the solvent was removed. Sucrose gradient centrifugation was performed to remove the excess lipid. Briefly, LCP NPs were loaded into a tube containing a sucrose density gradient ranging from 0% to 60% (w/w). After ultracentrifugation at 40,000 *g* for 3 h, excess lipids in the upper part of the gradient were separated from the dense LCP, which formed a sharp band around the 10–30% layer in the gradient. The morphology from each layer was confirmed by TEM.

Preparation of Tumor Models

Female nude mice (18–22 g) were inoculated subcutaneously with a combination of NIH3T3 (2.5×10^6 cells) and UMUC3 (5×10^6 cells), or with H460 (5×10^6 cells, 100 μL) to form the stroma-vessel phenotype tumor model, or with A375lu (5×10^6 cells, 100 μL) to form the tumor vessel phenotype tumor model. The 4T1 cells (5×10^5 cells, 50 μL) were orthotopically inoculated into the breast fat pads of the BALb/c mice and the D4M. 7A cells were injected intradermally (3×10^5 cells, 50 μL) into C57/B6 mice to form the stroma-vessel and tumor-vessel type models, respectively, in the syngeneic host.

Measurement of Binding Affinity of L-LCP NPs for UMUC3 and Activated NIH3T3

A modification of the method reported by Zhou *et al.* was performed to determine the binding affinity of LCP NPs to Sigma R expressing cells.[49] Briefly, 2×10^5 UMUC3 cells, NIH3T3 cells (activated with TGFβ 10 ng/mL, overnight), or GFP-positive fibroblasts sorted from the tumor tissues were incubated with various dilutions of DiI-labeled L-LCP NPs (±AA) at 4 °C for 40 min (concentration of NP ranges from 0.31 to 2.5 nM) in FACs buffer. Considering the similarities in surface properties of L-LCP to liposomes, the concentration

of LCP NPs was roughly converted from the concentration of phospholipid on the basis of the approximate number of phospholipid molecules per ~90 nm liposome (80,000).[49] Then the reaction was stopped by washing twice with FACs buffer. Afterward, the amount of cell-bound NPs was quantified by flow cytometry in BD FACs Machine. K_D values were determined by the following equation:

$$\mathrm{MFI} = \mathrm{MFI}_{\min} + \mathrm{MFI}_{\max}\left(\frac{[\mathrm{NP}]}{K_D + [\mathrm{NP}]}\right)$$

where MFI = mean fluorescence intensity, $\mathrm{MFI}_{\min}$ = background fluorescence, and $\mathrm{MFI}_{\max}$ was calculated from the plot. The term [NP] has been substituted for $[\mathrm{NP} - \mathrm{NP}_{\mathrm{bound}}]$, the unbound NP concentration, based on the assumption that the concentration of bound NP is much less than total NP.

Flow Cytometry Analysis

To study the kinetics of the intratumoral cell populations that took up NPs, DiI-labeled LCP NPs (S/L, ±AA) at a dose of 300 μg/kg DiI were intravenously administered into nude mice bearing UMUC3/3T3-GFP xenograft (tumor volume, 400–600 mm^3, n = 3–6 for each group). The mice were euthanized at determined time points, and tumor tissues were collected. Fresh tumor tissues were dissociated with the digestion solution to generate a single cell suspension. After red blood cell lysis, cells were washed with PBS and subjected to flow cytometry analysis. To study the nontarget LCPs NP (S/L) dispositions in 4T1, H460, D4M, and A375Lu at early time point, the same dose of DiI-LCP NPs was intravenously injected into mice bearing different tumors. Mice were sacrificed 8 h post-injection and subjected to the same treatment as mentioned above. After obtaining single cell suspensions, cells were fixed with 2% paraformaldehyde. For the staining of fibroblasts with PDGFRα, the fixed cells (5×10^6 cells/mL) were stained with APC antimouse PDGFRα antibody (BD bioscience, San Jose, CA) and processed following the manufacturer's instruction. For the staining of intracellular fibroblasts marker, αSMA, the cells from the tissues were penetrated with penetration buffer (BD, Franklin Lakes, NJ) following the manufacturer's instructions. The antimouse αSMA (Abcam, Cambridge, MA) and isotype control were then applied, followed by extensive washing and Fluor 647 conjugated antirabbit secondary (Abcam, Cambridge, MA) staining. All staining procedures were carefully compensated by flow cytometry. To analyze the expression of sigma R in tumor cells and fibroblasts and to evaluate how expression levels correlated with the DiI-LCP NPs' distribution, cells were stained with an anti-Sigma R antibody (Santa Cruz biotechnology, Inc.) following the same staining protocol. The UMUC3 cells were pretransfected with red fluorescence protein (RFP) and fibroblasts were pretransfected with green fluorescence protein (GFP) to define the cell populations (n = 3–6). The flow cytometry data were analyzed using FlowJo 7.6.1 (FLOWJO, Ashland, OR). The % of DiI-positive cells per cell population was calculated according to the following equation:

$$\%\ \text{of DiI positive cells per cell population} = \frac{\%\ \text{of}\left(DiI^{+}\ Cell\ population^{+}\right)\text{of the parent cells}}{\%\ \text{of}\left(DiI^{+}\ Cell\ population^{+} + DiI^{-}\ Cell\ population^{+}\right)\text{of the parent cells}}$$

Cell population indicates either 3T3-GFP, RFP-UMUC3, sigma R^+, or $CD45^+$ cell populations.

In Vitro NP Penetration in a Core–Shell 3D Tumor Spheroid Model

For evaluating the effects of the BSB elicited by fibroblasts *in vitro*, *ex vivo* multicellular core–shell 3D tumor spheroids mimicking the single tumor nest surrounded by fibroblasts were developed using the lipid overlay system with some adjustments.[50–53] This model was used to study the penetration behavior of LCP NPs after extravasating from the blood vessel. In brief, 1×10^4 UMUC3 cells were seeded into each well (using complete medium) of the ultralow attachment round-bottom 96 well plates (Costar, Corning, NY), followed by centrifugation at 900 rpm for 2 min to cluster the cells to the bottom of the wells and incubation at 37 °C for 4 days. The culture medium was changed every 2 days. Every fourth day, 1×10^4 GFP-NIH3T3 cells were added into each well, followed by continuous gentle rotation (200 rpm, 37 °C) for 6 h. Then the formed core–shell tumor spheroid was incubated for another 2 days. The structure of the core–shell spheroid was confirmed using a Zeiss LSM700 confocal microscope. Briefly, the spheroid was carefully transferred to a chambered coverslips and scanned from the bottom. Each scanning layer was 15 μm in thickness, and the total scanning was ~190 μm in depth. Only the samples with uniform and compact core–shell structure were selected for the follow-up studies (approximately 15 out of the 96 well-plate). For the time-lapse assay, fluorescence images were acquired at a fixed focus at determined time points. Radial fluorescence intensity profiles in the spheroids were generated using a customized script in ImageJ.[38] Average fluorescence intensity was determined for two annular regions: the tumor region (nonfluorescence) and the fibroblast region (fluorescence region).[38,53] The treated spheroids were also washed with PBS and dissociated with collagenase and trypsin. The DiI positive cell populations in both fibroblasts and tumor cells were quantified by flow cytometry.

Statistical Analysis

Data are presented as mean ± SD (standard deviation). A two-tailed Student's *t* test or a one-way analysis of variance (ANOVA) were performed when comparing two groups or larger than two groups, respectively. Statistical significance was defined as the P value <0.05. Statistical analysis was performed using Prism Software.

Supplementary Material

Refer to Web version on PubMed Central for supplementary material.

Acknowledgments

We acknowledge UNC Animal Histopathology Core and UNC Translational Pathology Laboratory for tissue embedding, IF, and IHC staining. We also appreciate the help of UNC Flow Cytometry Core and UNC CHANL for cell sorting and TEM imaging. The work was supported by NIH grants CA149363, CA151652, and CA149387 and by the North Carolina Biotech Center Institutional Support grant 2005-IDG-1016.

References

1. Juweid M, Neumann R, Paik C, Perez-Bacete MJ, Sato J, van Osdol W, Weinstein JN. Micropharmacology of Monoclonal Antibodies in Solid Tumors: Direct Experimental Evidence for a Binding Site Barrier. Cancer Res. 1992; 52:5144–5153. [PubMed: 1327501]
2. Weinstein JN, van Osdol W. Early Intervention in Cancer Using Monoclonal Antibodies and Other Biological Ligands: Micropharmacology and the “Binding Site Barrier”. Cancer Res. 1992; 52:2747s–2751s. [PubMed: 1563006]
3. Cheng Z, Al Zaki A, Hui JZ, Muzykantov VR, Tsourkas A. Multifunctional Nanoparticles: Cost versus Benefit of Adding Targeting and Imaging Capabilities. Science. 2012; 338:903–910. [PubMed: 23161990]
4. Lee H, Fonge H, Hoang B, Reilly RM, Allen C. The Effects of Particle Size and Molecular Targeting on the Intratumoral and Subcellular Distribution of Polymeric Nanoparticles. Mol Pharmaceutics. 2010; 7:1195–1208.
5. Song G, Darr DB, Santos CM, Ross M, Valdivia A, Jordan JL, Midkiff BR, Cohen S, Nikolaishvili-Feinberg N, Miller CR, Tarrant TK, Rogers AB, Dudley AC, Perou CM, Zamboni WC. Effects of Tumor Microenvironment Heterogeneity on Nanoparticle Disposition and Efficacy in Breast Cancer Tumor Models. Clin Cancer Res. 2014; 20:6083–6095. [PubMed: 25231403]
6. Sugimoto H, Mundel TM, Kieran MW, Kalluri R. Identification of Fibroblast Heterogeneity in the Tumor Microenvironment. Cancer Biol Ther. 2006; 5:1640–1646. [PubMed: 17106243]
7. Smith NR, Baker D, Farren M, Pommier A, Swann R, Wang X, Mistry S, McDaid K, Kendrew J, Womack C, Wedge SR, Barry ST. Tumor Stromal Architecture can Define the Intrinsic Tumor Response to VEGF-targeted Therapy. Clin Cancer Res. 2013; 19:6943–6956. [PubMed: 24030704]
8. Kano MR, Bae Y, Iwata C, Morishita Y, Yashiro M, Oka M, Fujii T, Komuro A, Kiyono K, Kaminishi M, Hirakawa K, Ouchi Y, Nishiyama N, Kataoka K, Miyazono K. Improvement of Cancer-Targeting Therapy, Using Nanocarriers for Intractable Solid Tumors by Inhibition of TGF-beta Signaling. Proc Natl Acad Sci U S A. 2007; 104:3460–3465. [PubMed: 17307870]
9. Nishihara H. Human Pathological Basis of Blood Vessels and Stromal Tissue for Nanotechnology. Adv Drug Delivery Rev. 2014; 74:19–27.
10. Navab R, Strumpf D, Bandarchi B, Zhu CQ, Pintilie M, Ramnarine VR, Ibrahimov E, Radulovich N, Leung L, Barczyk M, Panchal D, To C, Yun JJ, Der S, Shepherd FA, Jurisica I, Tsao MS. Prognostic Gene-Expression Signature of Carcinoma-Associated Fibroblasts in Non-Small Cell Lung Cancer. Proc Natl Acad Sci U S A. 2011; 108:7160–7165. [PubMed: 21474781]
11. Yamashita M, Ogawa T, Zhang X, Hanamura N, Kashikura Y, Takamura M, Yoneda M, Shiraishi T. Role of Stromal Myofibroblasts in Invasive Breast Cancer: Stromal Expression of Alpha-smooth Muscle Actin Correlates with Worse Clinical Outcome. Breast Cancer. 2012; 19:170–176. [PubMed: 20978953]
12. Cheng L, Montironi R, Davidson DD, Lopez-Beltran A. Staging and Reporting of Urothelial Carcinoma of the Urinary Bladder. Mod Pathol. 2009; 22:S70–95. [PubMed: 19494855]
13. Ohlund D, Elyada E, Tuveson D. Fibroblast Heterogeneity in the Cancer Wound. J Exp Med. 2014; 211:1503–1523. [PubMed: 25071162]
14. Kalluri R, Zeisberg M. Fibroblasts in Cancer. Nat Rev Cancer. 2006; 6:392–401. [PubMed: 16572188]
15. Murakami M, Ernsting MJ, Undzys E, Holwell N, Foltz WD, Li SD. Docetaxel Conjugate Nanoparticles that Target Alpha-Smooth Muscle Actin-Expressing Stromal Cells Suppress Breast Cancer Metastasis. Cancer Res. 2013; 73:4862–4871. [PubMed: 23907638]

16. Zhang J, Miao L, Guo S, Zhang Y, Zhang L, Satterlee A, Kim WY, Huang L. Synergistic Anti-tumor Effects of Combined Gemcitabine and Cisplatin Nanoparticles in a Stroma-Rich Bladder Carcinoma Model. J Controlled Release. 2014; 182:90–96.
17. Ozdemir BC, Pentcheva-Hoang T, Carstens JL, Zheng X, Wu CC, Simpson TR, Laklai H, Sugimoto H, Kahlert C, Novitskiy SV, De Jesus-Acosta A, Sharma P, Heidari P, Mahmood U, Chin L, Moses HL, Weaver VM, Maitra A, Allison JP, LeBleu VS, Kalluri R. Depletion of Carcinoma-Associated Fibroblasts and Fibrosis Induces Immunosuppression and Accelerates Pancreas Cancer with Reduced Survival. Cancer Cell. 2014; 25:719–734. [PubMed: 24856586]
18. Gore J, Korc M. Pancreatic Cancer Stroma: Friend or Foe? Cancer Cell. 2014; 25:711–712. [PubMed: 24937454]
19. Rhim AD, Oberstein PE, Thomas DH, Mirek ET, Palermo CF, Sastra SA, Dekleva EN, Saunders T, Becerra CP, Tattersall IW, Westphalen CB, Kitajewski J, Fernandez-Barrena MG, Fernandez-Zapico ME, Iacobuzio-Donahue C, Olive KP, Stanger BZ. Stromal Elements Act to Restrain, Rather than Support, Pancreatic Ductal Adenocarcinoma. Cancer Cell. 2014; 25:735–747. [PubMed: 24856585]
20. Miao L, Wang Y, Lin CM, Xiong Y, Chen N, Zhang L, Kim WY, Huang L. Nanoparticle Modulation of the Tumor Microenvironment Enhances Therapeutic Efficacy of Cisplatin. J Controlled Release. 2015; 217:27–41.
21. Sun Y, Campisi J, Higano C, Beer TM, Porter P, Coleman I, True L, Nelson PS. Treatment-induced Damage to the Tumor Microenvironment Promotes Prostate Cancer Therapy Resistance through WNT16B. Nat Med. 2012; 18:1359–1368. [PubMed: 22863786]
22. Liu Y, Hu Y, Huang L. Influence of Polyethylene Glycol Density and Surface Lipid on Pharmacokinetics and Biodistribution of Lipid-Calcium-Phosphate Nanoparticles. Biomaterials. 2014; 35:3027–3034. [PubMed: 24388798]
23. Li J, Yang Y, Huang L. Calcium Phosphate Nanoparticles with an Asymmetric Lipid Bilayer Coating for siRNA Delivery to the Tumor. J Controlled Release. 2012; 158:108–114.
24. Zhang Y, Schwerbrock NM, Rogers AB, Kim WY, Huang L. Codelivery of VEGF siRNA and Gemcitabine Monophosphate in a Single Nanoparticle Formulation for Effective Treatment of NSCLC. Mol Ther. 2013; 21:1559–1569. [PubMed: 23774791]
25. Hu Y, Haynes MT, Wang Y, Liu F, Huang L. A Highly Efficient Synthetic Vector: Nonhydrodynamic Delivery of DNA to Hepatocyte Nuclei *in vivo*. ACS Nano. 2013; 7:5376–5384. [PubMed: 23647441]
26. Tseng YC, Xu Z, Guley K, Yuan H, Huang L. Lipid-Calcium Phosphate Nanoparticles for Delivery to the Lymphatic System and SPECT/CT Imaging of Lymph Node Metastases. Biomaterials. 2014; 35:4688–4698. [PubMed: 24613050]
27. Banerjee R, Tyagi P, Li S, Huang L. Anisamide-Targeted Stealth Liposomes: a Potent Carrier for Targeting Doxorubicin to Human Prostate Cancer Cells. Int J Cancer. 2004; 112:693–700. [PubMed: 15382053]
28. Cabral H, Matsumoto Y, Mizuno K, Chen Q, Murakami M, Kimura M, Terada Y, Kano MR, Miyazono K, Uesaka M, Nishiyama N, Kataoka K. Accumulation of Sub-100 nm Polymeric Micelles in Poorly Permeable Tumours Depends on Size. Nat Nanotechnol. 2011; 6:815–823. [PubMed: 22020122]
29. Lee H, Hoang B, Fonge H, Reilly RM, Allen C. *In vivo* Distribution of Polymeric Nanoparticles at the Whole-Body, Tumor, and Cellular Levels. Pharm Res. 2010; 27:2343–2355. [PubMed: 20195708]
30. Park SY, Kim HM, Koo JS. Differential Expression of Cancer-associated fibroblast-related Proteins according to Molecular Subtype and Stromal Histology in Breast Cancer. Breast Cancer Res Treat. 2015; 149:727–741. [PubMed: 25667103]
31. Marsh T, Pietras K, McAllister SS. Fibroblasts as Architects of Cancer Pathogenesis. Biochim Biophys Acta, Mol Basis Dis. 2013; 1832:1070–1078.
32. Guo S, Wang Y, Miao L, Xu Z, Lin CM, Zhang Y, Huang L. Lipid-Coated Cisplatin Nanoparticles Induce Neighboring Effect and Exhibit Enhanced Anticancer Efficacy. ACS Nano. 2013; 7(11): 9896–9904. [PubMed: 24083505]

33. Baxter LT, Jain RK. Transport of Fluid and Macromolecules in Tumors. III. Role of Binding and Metabolism. Microvasc Res. 1991; 41:5–23. [PubMed: 2051954]
34. Kirpotin DB, Drummond DC, Shao Y, Shalaby MR, Hong K, Nielsen UB, Marks JD, Benz CC, Park JW. Antibody Targeting of Long-Circulating Lipidic Nanoparticles does not Increase Tumor Localization but does Increase Internalization in Animal Models. Cancer Res. 2006; 66:6732–6740. [PubMed: 16818648]
35. Chauhan VP, Jain RK. Strategies for Advancing Cancer Nanomedicine. Nat Mater. 2013; 12:958–962. [PubMed: 24150413]
36. He C, Hu Y, Yin L, Tang C, Yin C. Effects of Particle Size and Surface Charge on Cellular Uptake and Biodistribution of Polymeric Nanoparticles. Biomaterials. 2010; 31:3657–3666. [PubMed: 20138662]
37. Gao H, Shi W, Freund LB. Mechanics of Receptor-Mediated Endocytosis. Proc Natl Acad Sci U S A. 2005; 102:9469–9474. [PubMed: 15972807]
38. Kim B, Han G, Toley BJ, Kim CK, Rotello VM, Forbes NS. Tuning Payload Delivery in Tumour Cylindroids using Gold Nanoparticles. Nat Nanotechnol. 2010; 5(6):465–472. [PubMed: 20383126]
39. Stylianopoulos T, Poh MZ, Insin N, Bawendi MG, Fukumura D, Munn LL, Jain RK. Diffusion of Particles in the Extracellular Matrix: the Effect of Repulsive Electrostatic Interactions. Biophys J. 2010; 99:1342–1349. [PubMed: 20816045]
40. van Waarde A, Rybczynska AA, Ramakrishnan NK, Ishiwata K, Elsinga PH, Dierckx RA. Potential Applications for Sigma Receptor Ligands in Cancer Diagnosis and Therapy. Biochim Biophys Acta, Biomembr. 2015; 1848:2703–2714.
41. Parker N, Turk MJ, Westrick E, Lewis JD, Low PS, Leamon CP. Folate Receptor Expression in Carcinomas and Normal Tissues Determined by a Quantitative Radioligand Binding Assay. Anal Biochem. 2005; 338:284–293. [PubMed: 15745749]
42. Prutki M, Poljak-Blazi M, Jakopovic M, Tomas D, Stipancic I, Zarkovic N. Altered Iron Metabolism, Transferrin Receptor 1 and Ferritin in Patients with Colon Cancer. Cancer Lett. 2006; 238:188–196. [PubMed: 16111806]
43. Stylianopoulos T, Jain RK. Combining Two Strategies to Improve Perfusion and Drug Delivery in Solid Tumors. Proc Natl Acad Sci U S A. 2013; 110:18632–18637. [PubMed: 24167277]
44. Huang K, Ma H, Liu J, Huo S, Kumar A, Wei T, Zhang X, Jin S, Gan Y, Wang PC, He S, Zhang X, Liang XJ. Size-dependent Localization and Penetration of Ultrasmall Gold Nano-particles in Cancer Cells, Multicellular Spheroids, and Tumors *in vivo*. ACS Nano. 2012; 6:4483–4493. [PubMed: 22540892]
45. Reuter KG, Perry JL, Kim D, Luft JC, Liu R, DeSimone JM. Targeted PRINT Hydrogels: The Role of Nanoparticle Size and Ligand Density on Cell Association, Biodistribution, and Tumor Accumulation. Nano Lett. 2015; 15:6371–6378. [PubMed: 26389971]
46. Li SD, Huang L. Stealth Nanoparticles: High Density but Sheddable PEG is a Key for Tumor Targeting. J Controlled Release. 2010; 145:178–181.
47. Sherman MH, Yu RT, Engle DD, Ding N, Atkins AR, Tiriac H, Collisson EA, Connor F, Van Dyke T, Kozlov S, Martin P, Tseng TW, Dawson DW, Donahue TR, Masamune A, Shimosegawa T, Apte MV, Wilson JS, Ng B, Lau SL, et al. Vitamin D Receptor-mediated Stromal Reprogramming Suppresses Pancreatitis and Enhances Pancreatic Cancer Therapy. Cell. 2014; 159:80–93. [PubMed: 25259922]
48. Whatcott CJ, Han H, Von Hoff DD. Orchestrating the Tumor Microenvironment to Improve Survival for Patients With Pancreatic Cancer: Normalization, Not Destruction. Cancer J. 2015; 21:299–306. [PubMed: 26222082]
49. Zhou Y, Drummond DC, Zou H, Hayes ME, Adams GP, Kirpotin DB, Marks JD. Impact of Single-Chain Fv Antibody Fragment Affinity on Nanoparticle Targeting of Epidermal Growth Factor Receptor-Expressing Tumor Cells. J Mol Biol. 2007; 371:934–947. [PubMed: 17602702]
50. Hirschhaeuser F, Menne H, Dittfeld C, West J, Mueller-Klieser W, Kunz-Schughart LA. Multicellular Tumor Spheroids: an Underestimated Tool is Catching up again. J Biotechnol. 2010; 148:3–15. [PubMed: 20097238]

51. Infanger DW, Lynch ME, Fischbach C. Engineered Culture Models for Studies of Tumor-microenvironment Interactions. Annu Rev Biomed Eng. 2013; 15:29–53. [PubMed: 23642249]

52. Fischbach C, Chen R, Matsumoto T, Schmelzle T, Brugge JS, Polverini PJ, Mooney DJ. Engineering Tumors with 3D Scaffolds. Nat Methods. 2007; 4:855–860. [PubMed: 17767164]

53. Jiang X, Xin H, Gu J, Xu X, Xia W, Chen S, Xie Y, Chen L, Chen Y, Sha X, Fang X. Solid Tumor Penetration by Integrin-Mediated Pegylated Poly(Trimethylene Carbonate) Nano-particles Loaded with Paclitaxel. Biomaterials. 2013; 34:1739–1746. [PubMed: 23211449]

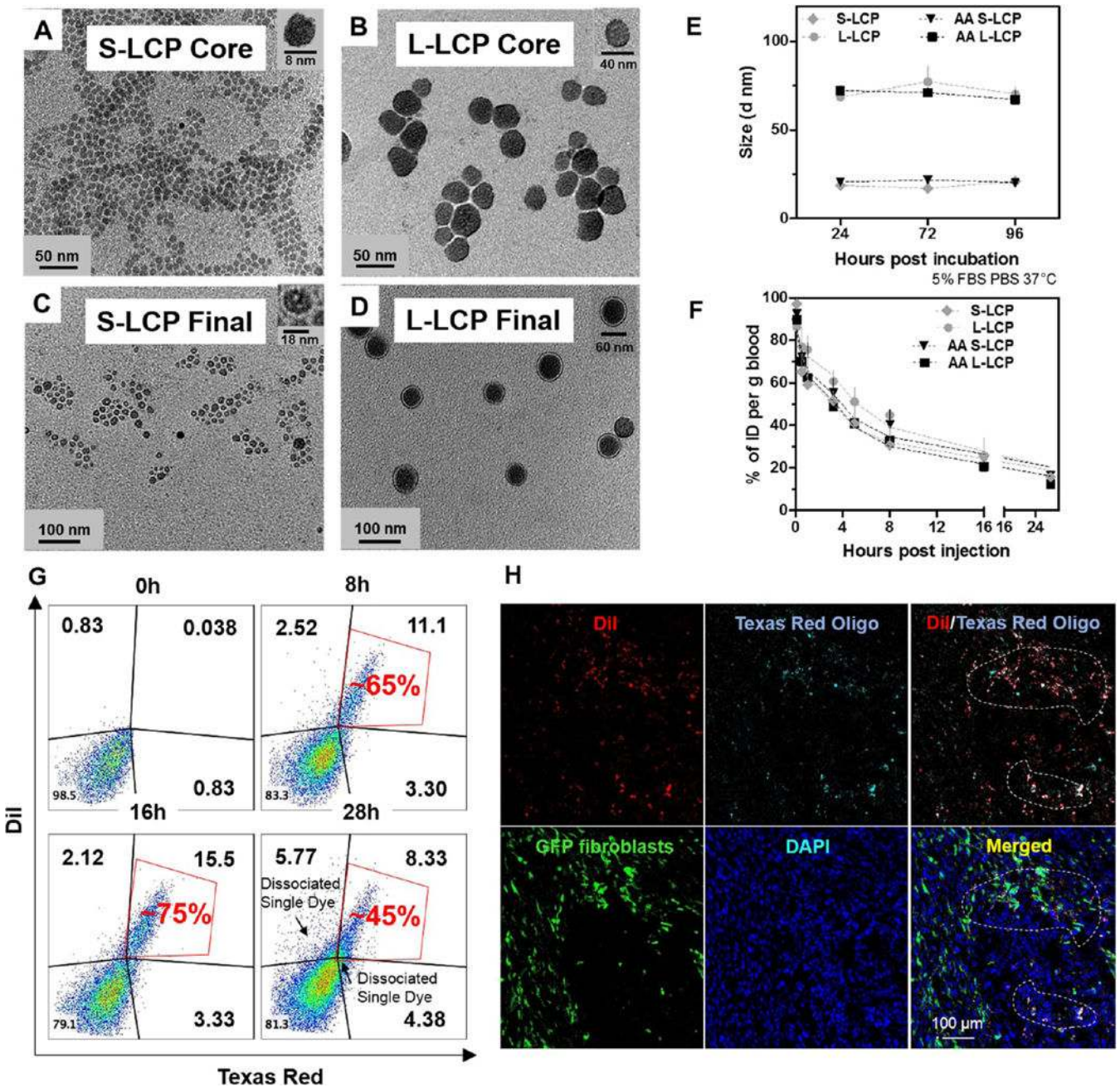

Figure 1.

Characterization of LCP NPs. (A,B) Representative TEM images of LCP cores (S/L). (C,D) TEM images of final LCP NPs (S/L). (E) *In vitro* stability of LCP NPs (S/L, ±AA) in 5% FBS, 37 °C, over 96 h. (F) PK profiles of LCP NPs (S/L, ±AA). (G) Co-association of DiI and Texas Red Oligo in the same cells within the UMUC3/3T3-GFP tumor models 8, 16, and 28 h after double fluorescence-labeled NPs injection. Data were analyzed by flow cytometry, and the fluorescence was compensated. The red-marked population indicates the % of double positive cells in all fluorescence positive cells. (H) Fluorescence images of DiI/ Texas Red Oligo-labeled LCP NPs in the GFP positive fibroblasts 8 h post-injection of the

UMUC3/3T3-GFP tumors. The circled (white dot) population indicates the double fluorescences (DiI and Texas Red) in GFP-fibroblasts (upper circles) or nonfibroblast cells (lower circles) (cryosection).

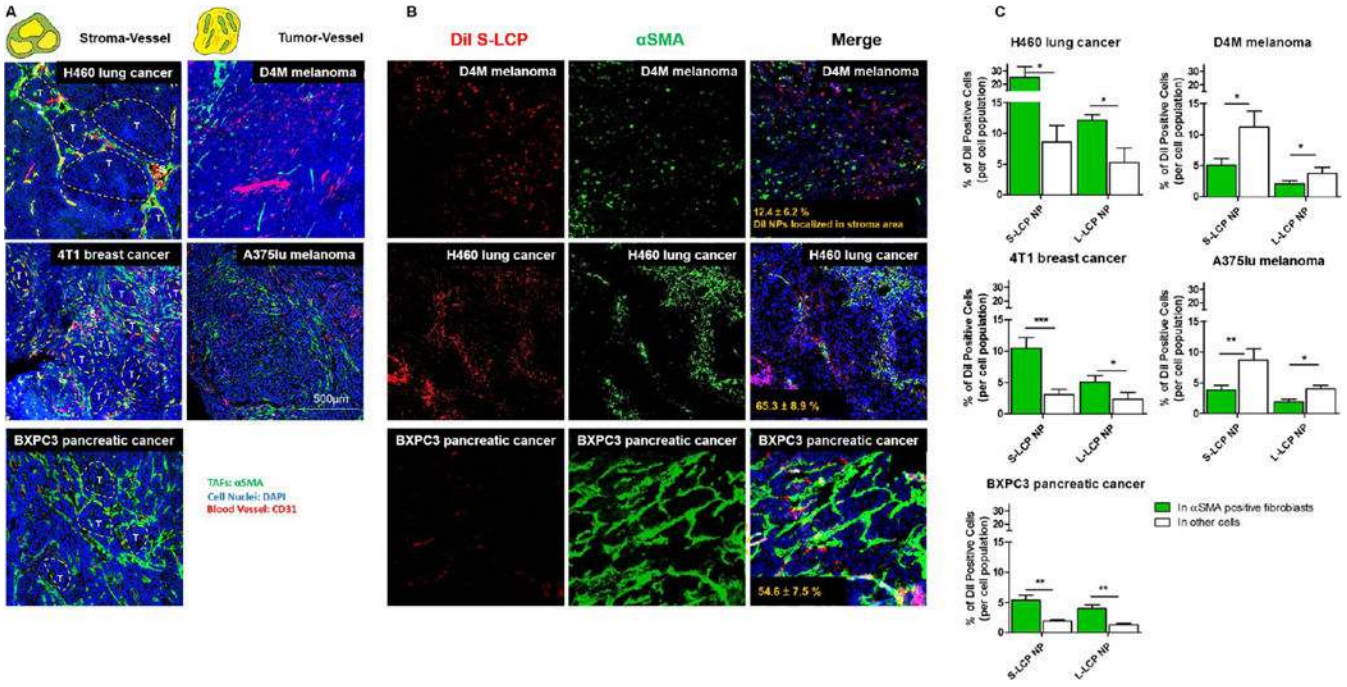

Figure 2.

Stroma-vessel architecture affects the intratumoral distribution of nontargeted NPs. (A) Immunostaining of CD31 (red for blood vessels) and αSMA (green for fibroblasts) in subcutaneous tumor models (paraffin sections) with different tumor-stroma architectures. H460, 4T1, and BXPC3 belong to the stroma-vessel phenotype. Tumor nests (T) are highlighted in the images. D4M and A375lu belong to tumor- vessel phenotype. (B) Confocal images of DiI-labeled NP distribution in D4M, H460, and BXPC3 8 h post-injection (cryosections). The fibroblasts were visualized by staining with αSMA. (C) Flow cytometry analysis of the association of nontargeted DiI-labeled NPs with either αSMA-positive fibroblasts or other nonlabeled cells 8 h post-injection in the four different tumors (n = 3; * P < 0.05; ** P < 0.01; *** P < 0.001).

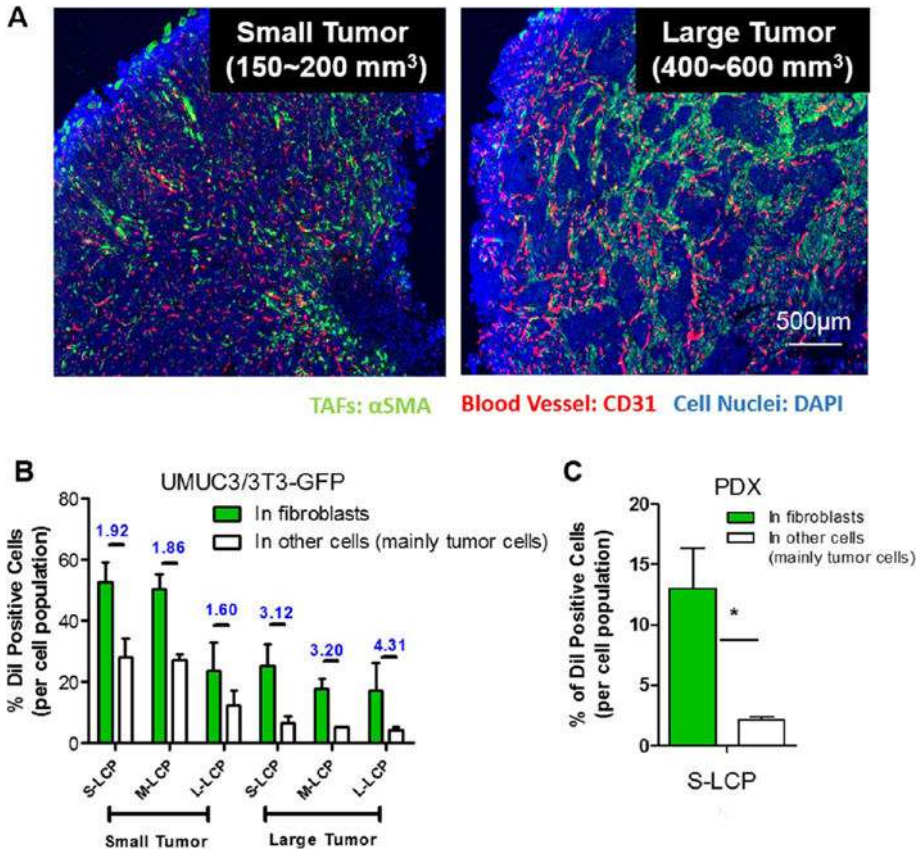

Figure 3.

UMUC3/3T3 recapitulates NP distribution patterns in desmoplastic tumors. (A) A tumor model established by co-inoculating UMUC3 with GFP-transfected fibroblasts NIH3T3 (UMUC3/3T3-GFP). When the tumor was small, it mainly adopted a tumor-vessel phenotype in most areas. As the tumor grew, it adopted a stroma-vessel phenotype. (B) Flow cytometry analysis of the cellular distribution of nontargeted NPs (S-LCP NP, 18 nm; M-LCP NP, 35 nm (characterization not shown); L-LCP NP, 75 nm) ($n = 6$). Flow cytometry analysis of the association of S-LCP NPs in a bladder cancer PDX model 8 h post-injection ($n = 3$). The ratios of DiI-positive fibroblasts and other cells are calculated and shown in blue. * $P < 0.05$; ** $P < 0.01$; ns, no significant difference.

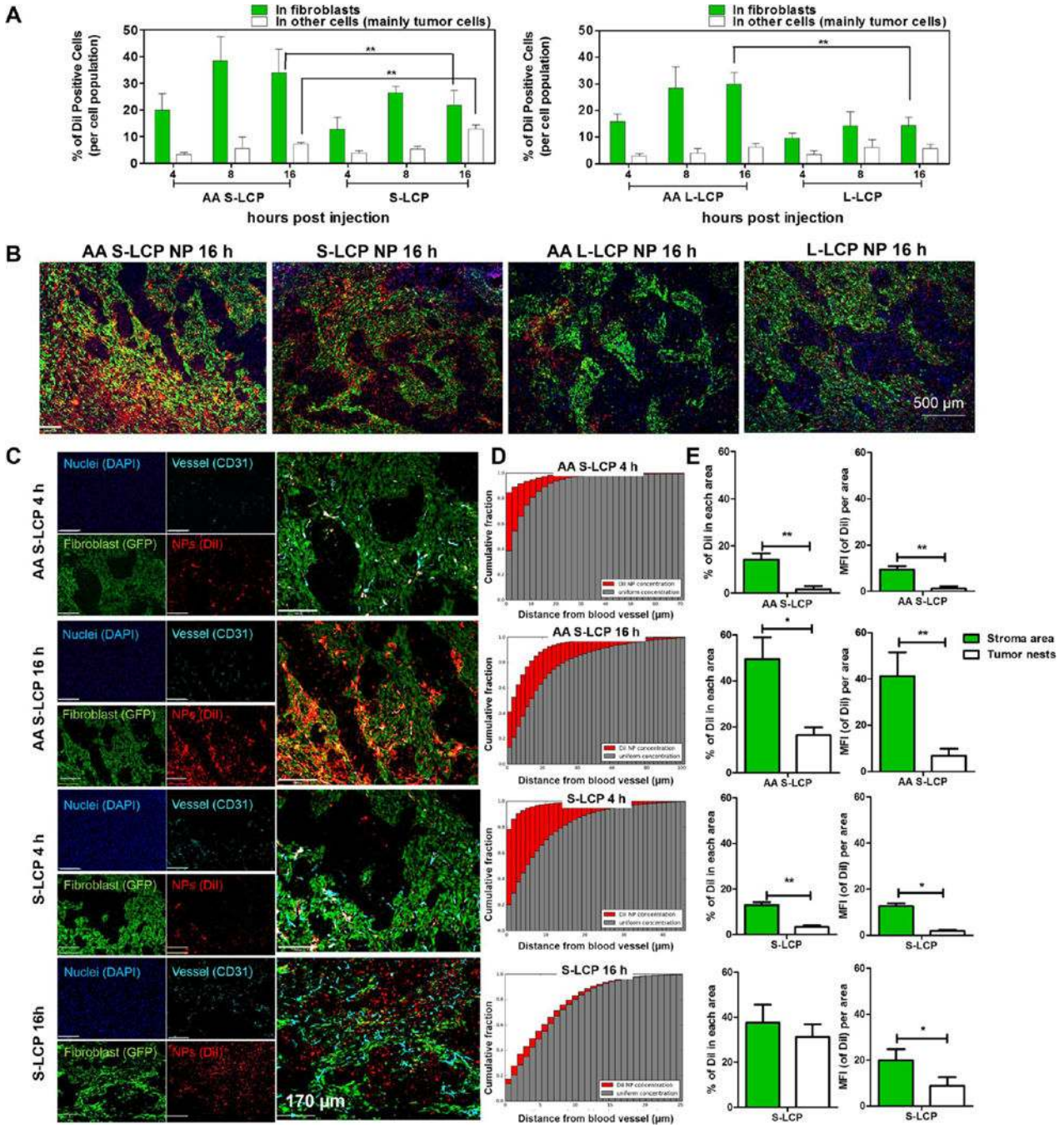

Figure 4.

Time-dependent association of nontargeted and targeted NPs in fibroblasts and other cells (mainly tumor cells). (A) Flow cytometry analysis of the time-dependent cellular distribution of NPs (S/L, ±AA) ($n = 6$, **, $P < 0.01$). (B) Representative low-magnification fluorescent images of DiI NPs distribution in tumor sections 16 h post-injection. Green: 3T3-GFP, red: DiI NPs. (C) Higher-magnification fluorescence images of S-LCP NP (with or without AA) at 4 or 16 h post-injection. Cyan: blood vessel. The accumulative distance of DiI NPs to the nearest CD31 positive blood vessels were quantified (D). In order to

quantitatively compare results from different samples, we compute the distance histogram for a uniform concentration of hypothetical particles (gray). Quantification (by ImageJ) of the mean fluorescence intensity (MFI) of DiI (left) or % of DiI positive (right) in the GFP- stroma area and tumor nests area are quantified in (E) ($n = 4$; * $P < 0.05$; ** $P < 0.01$).

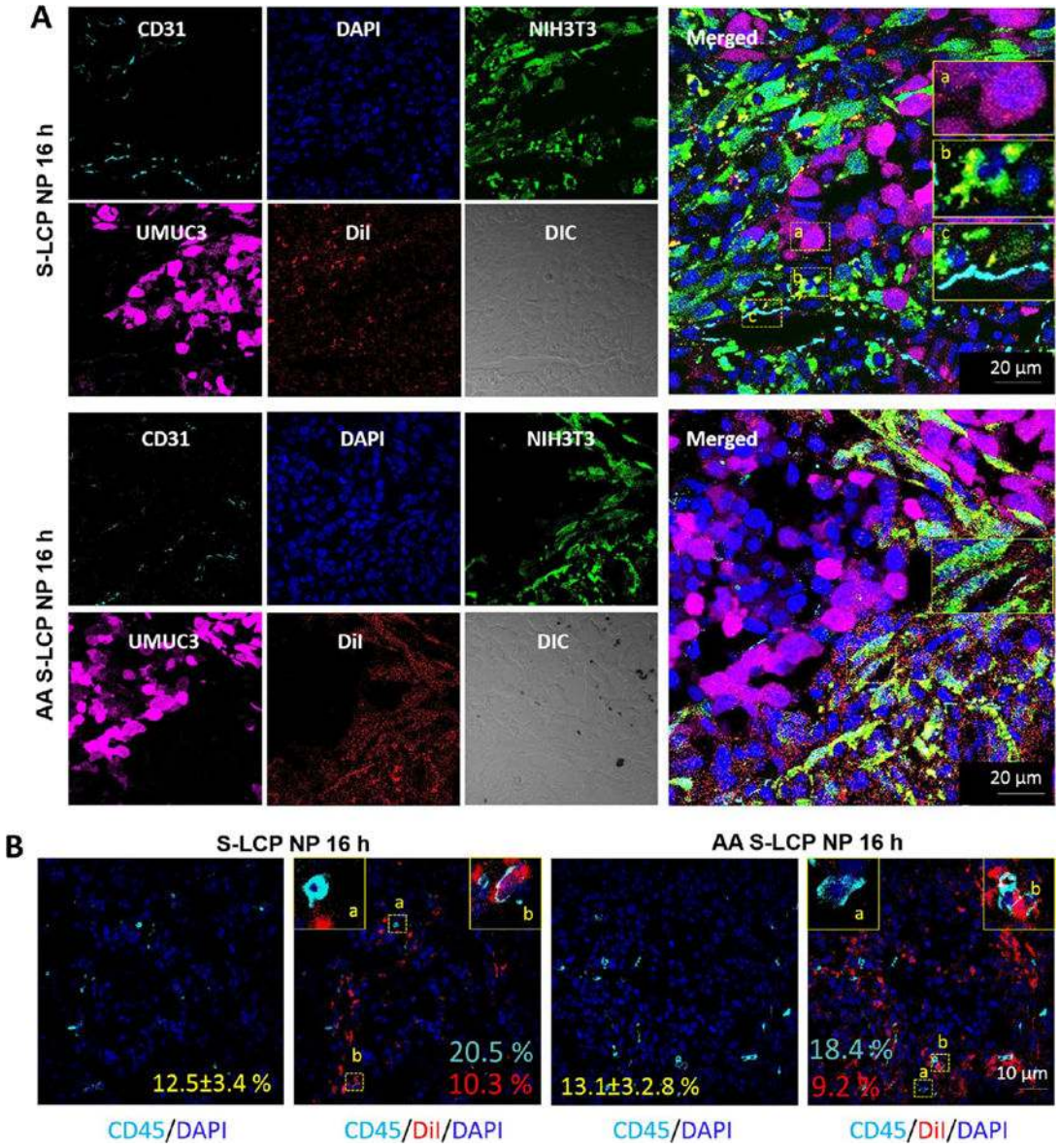

Figure 5.

Confocal analysis of the cellular association of S-LCP NPs (with or without AA, DiI labeled) 16 h after i.v. administration in UMUC3/3T3 xenografts. (A) Distribution of S-LCP NPs (with or without AA) in UMUC3- GFP tumor cells (magenta), 3T3-RFP fibroblasts (green), and CD31 endothelial cells (cyan). Single color panels on the left. Merged images are shown on the right. Particular areas are magnified for clear visualization (yellow dotted rectangle). Red arrows indicate the representative association of NPs with fibroblasts, white arrows indicate the representative association of NPs with tumor cells, and cyan arrows indicate endothelial outline. Nontargeted NPs showed scattered distributions in both fibroblasts and tumor cells. Fewer NPs are associated with the endothelial outline. (B) Distribution of NPs in CD45 positive leukocytes (cyan). Yellow numbers indicate the % of CD45 positive cells among all cell populations (mean ± SD). Cyan numbers quantify the % of CD45 positive cells that have taken up NPs (mean ± SD). Red numbers quantify the % of

DiI (NPs) positive cells that are leucocytes (mean ± SD). Both nontargeted and targeted NPs can be internalized by the leucocytes.

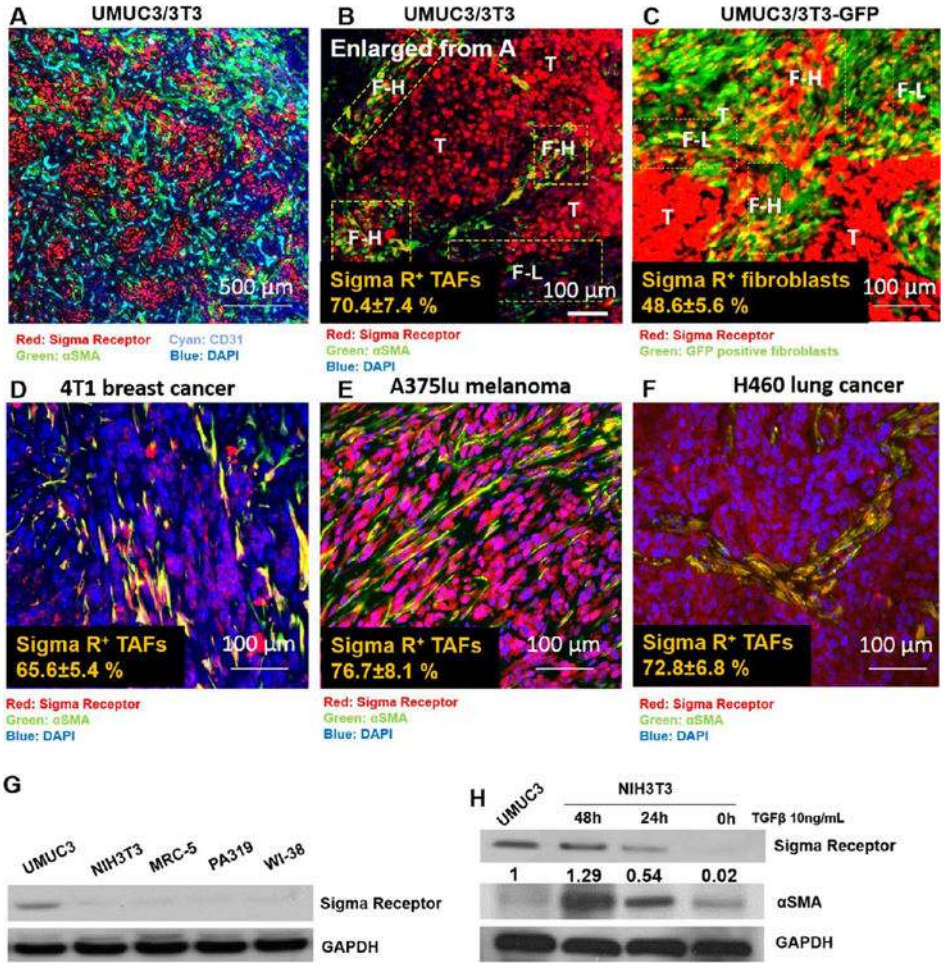

Figure 6.

Sigma receptor is expressed in αSMA positive TAFs. (A) IF staining of paraffin embedded tumor sections from the UMUC3/3T3 model. Red: Sigma R; green: αSMA; and cyan: CD31. Co-localization was observed partially between Sigma R and αSMA and illustrated as orange or yellow. (B) Higher magnification of the UMUC3/3T3 model stained with Sigma R and αSMA. The Sigma R high and low regions in fibroblasts were marked as F–H and F–L. Tumor nest (T) was highly positive for Sigma R. (C) Cryosections of UMUC3/3T3. Green indicated GFP-positive fibroblasts, and red indicated Sigma R. (D–F) Costaining of Sigma R (red) and αSMA (green) in 4T1, A375lu, and H460. The % of Sigma R positive fibroblasts or TAFs (αSMA) were quantified by ImageJ ($n = 3$). (G,H) Western blot analysis of Sigma R expression *in vitro* on different cell lines (including tumor cells UMUC3, and other mouse or human fibroblasts). Note that activation of NIH3T3 with TGFβ enhances the expression of Sigma R. The numbers below Western blot of Sigma R indicate the average intensity (quantified by ImageJ) of the blot in each samples compared to UMUC3 (set as 1).

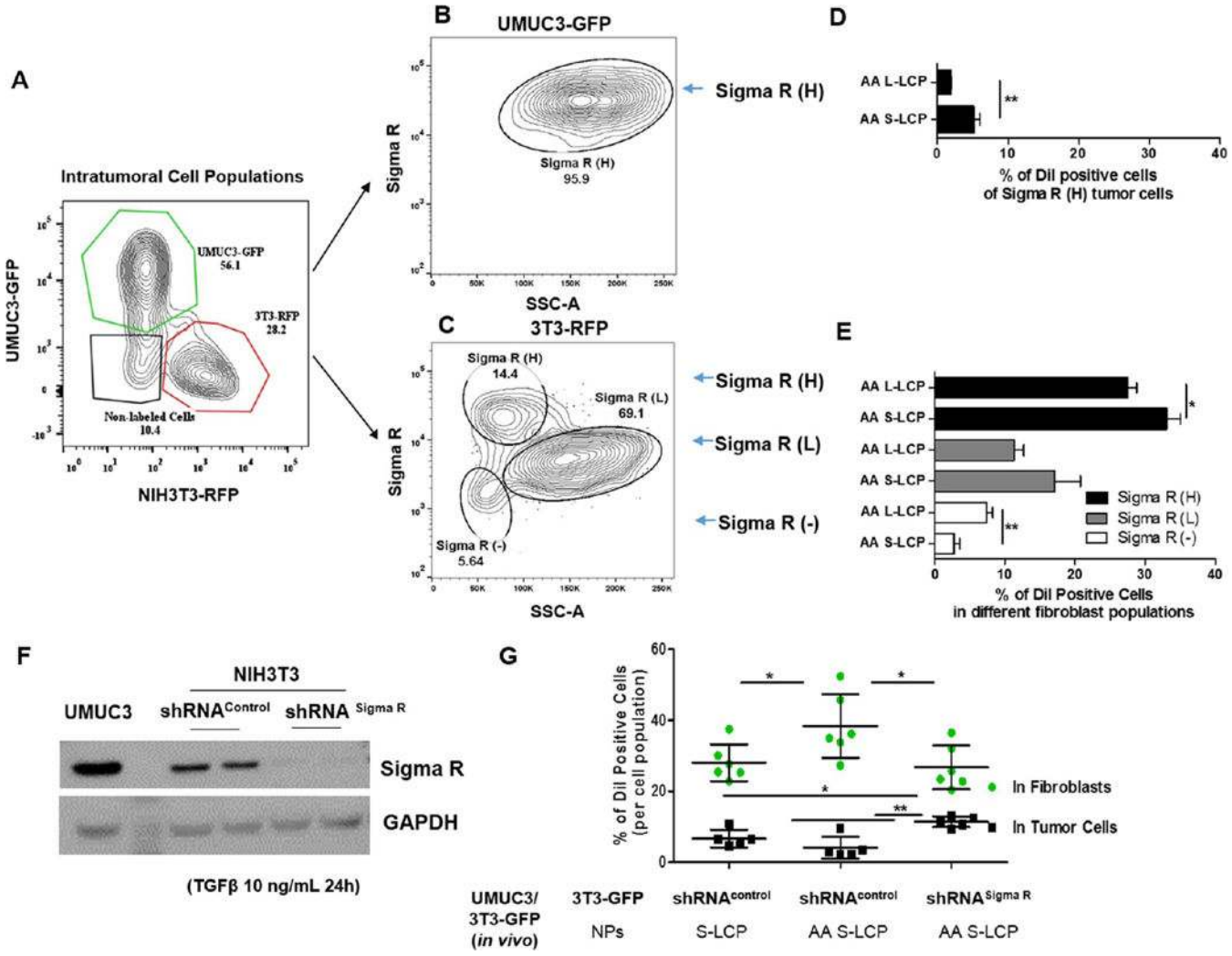

Figure 7.

Correlation between Sigma R level and distribution of targeted NPs. (A) Gating of UMUC3-GFP and 3T3-RFP in dissociated tumor tissues. (B,C) Gating of Sigma R positive populations in tumor cells and fibroblasts. Isotype controls are shown in Supporting Information figures. Most tumor cells have high and coherent Sigma R expressions, whereas, fibroblasts can be classified into Sigma R (H), Sigma R (L), and Sigma R (−) groups based on the expression of Sigma R levels. (D,E) Quantitative flow analysis of the distribution of DiI AA-NPs in different groups (different Sigma R level) of cells. (F) Western blot confirmation of the shRNA knockout of Sigma R in the NIH3T3 fibroblasts *in vitro*. (G) % of DiI positive cells in tumor cells and fibroblasts 8 h after injection of DiI NPs in the normal UMUC3/3T3-GFP model or UMUC3/3T3-GFP Sigma R knockout model (n = 6). * $P < 0.05$; ** $P < 0.001$.

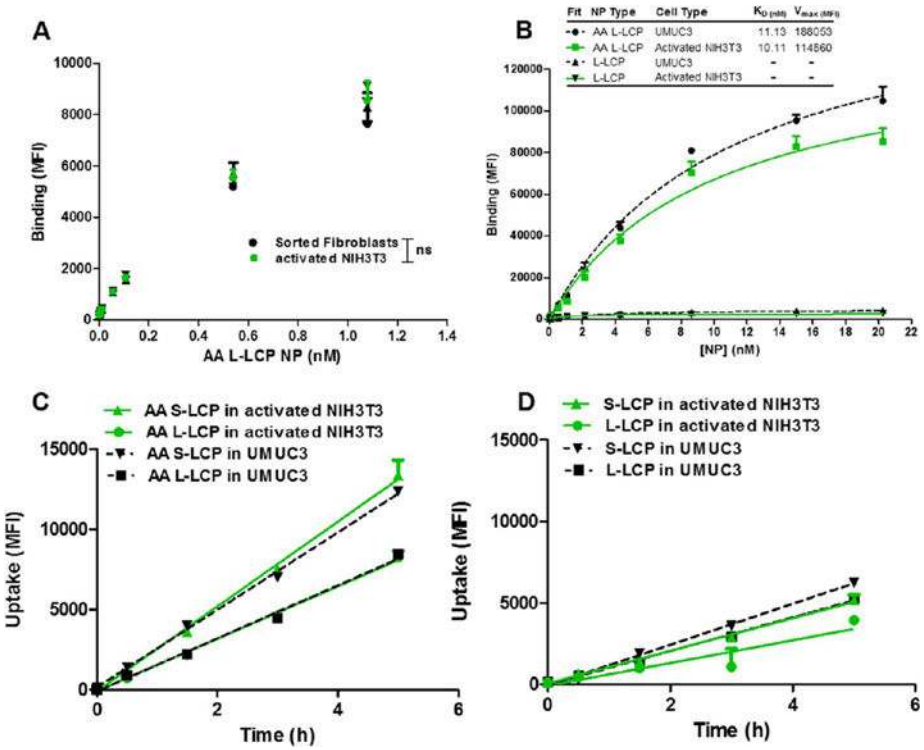

Figure 8.

Binding affinity and uptake rate of LCP NPs (S/L, ±AA) in UMUC3 and activated fibroblasts. (A) Binding curve of AA L-LCP NPs for activated NIH3T3 and sorted GFP-fibroblasts from the stroma-rich bladder tumor models. (B) Binding affinity of LCP NPs (S/L, ±AA) in UMUC3 and activated NIH3T3. The data points were fitted to Michaels–Menten curve, K_D, and V_{max} were calculated and shown in the chart. Time-dependent uptake of 1 nM LCP NPs (S/L) with or without AA in activated NIH3T3 and UMUC3 is shown in (C) and (D), respectively ($n = 3$).

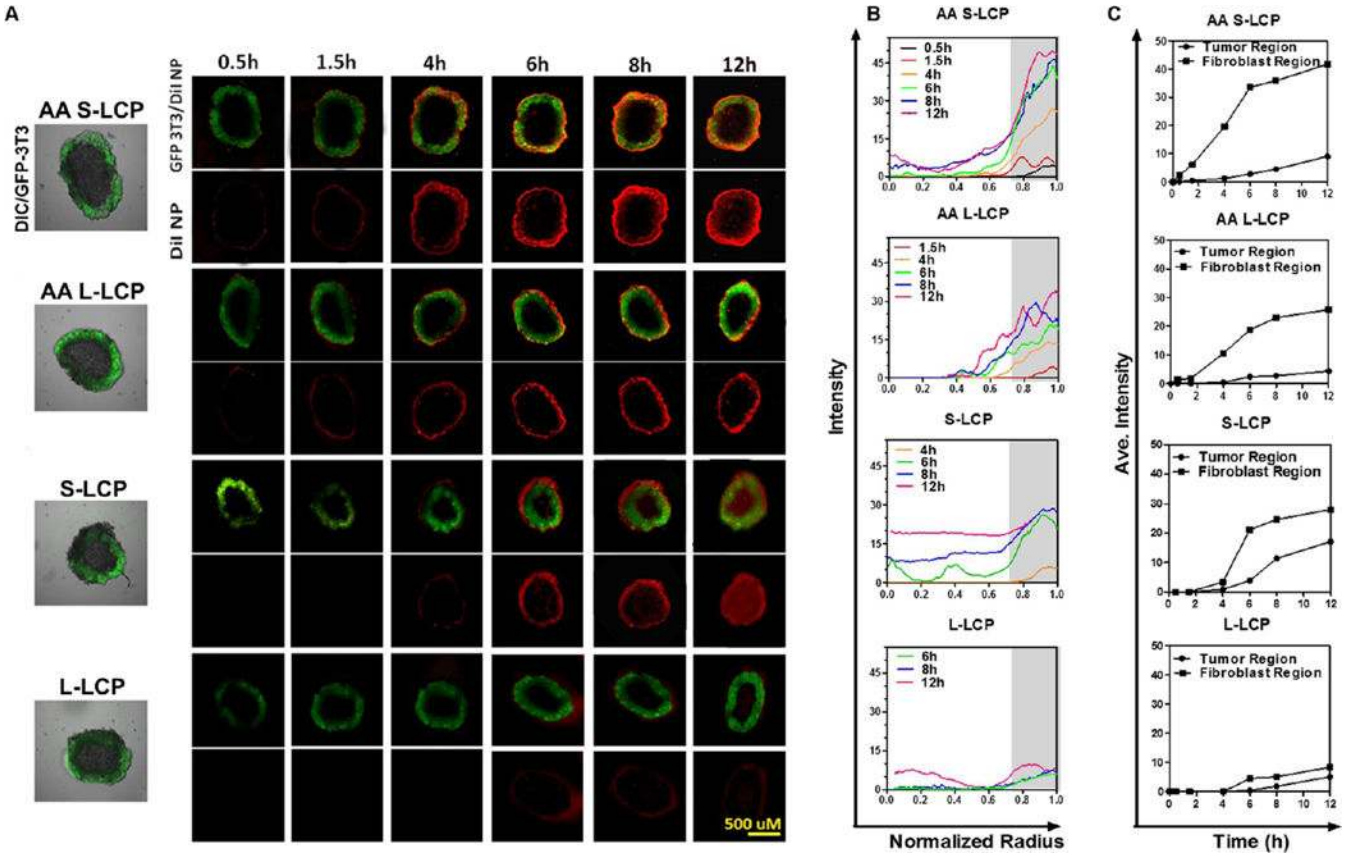

Figure 9.

Penetration, binding, and internalization kinetics of LCP NP (L/S, ±AA) in a core–shell *ex vivo* spheroid model. The core–shell 3D spheroid model was established by coating the UMUC3 spheroid with 3T3-GFP fibroblasts. Fluorescence images were acquired after incubation with DiI-labeled LCP NPs for determined time points and shown in (A). Scale bar, 500 μm. The corresponding fluorescence intensity profiles are shown at determined time points in (B). The gray zone indicates the position of fibroblasts. Change of average fluorescence intensities over time in the tumor region and the fibroblast region after incubation with DiI-labeled LCP NP are shown in (C). Mean value was presented ($n = 3$).

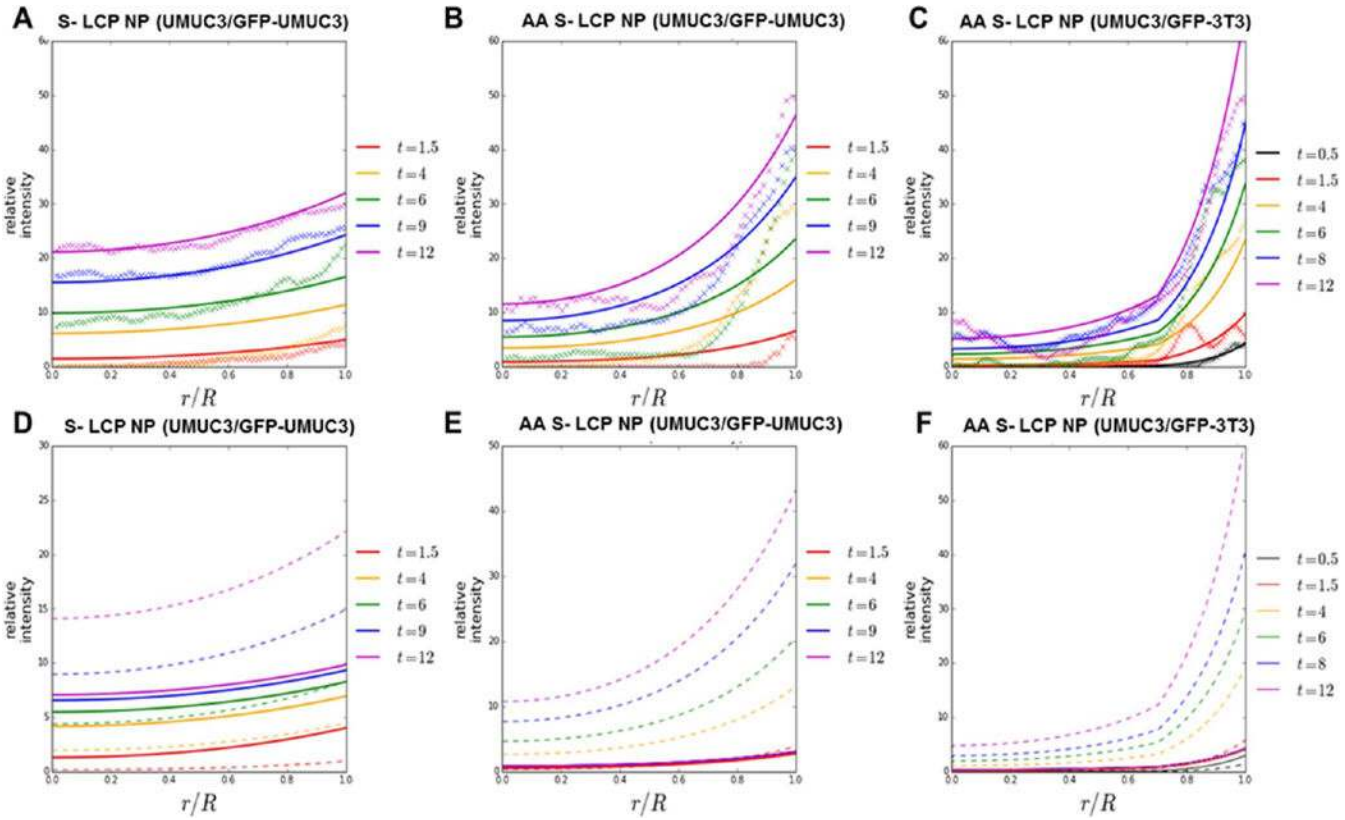

Figure 10.

Mathematical modeling of S-LCP NPs (±AA) distribution in the core–shell spheroid and predictions of cellular uptake of S-LCP NPs (±AA) (A–C) Fluorescence intensity profiles measured in fluorescence images of core–shell 3D spheroids (symbols), and those predicted by the mathematical model (solid lines). (D–F) Predictions of cellular associated NPs (dashed lines) and acellular NPs (solid lines).